ADVANCED FUNCTIONAL MATERIALS
www.afm-journal.de

Enhanced Cycle Stability of Low-Cost Na-Rich Metallic NaCl Electrode for Advanced Na-Ion Batteries

Iqra Moeez, Dieky Susanto, Jae-Ho Park, Ji-Young Kim, Hee-Dae Lim, and Kyung Yoon Chung**

Sodium-rich metallic Na_{x+z} has received significant attention as a low-cost alternative to the conventional electrode materials used in Li-ion batteries. However, the poor cyclability of Na_xCl remains a major challenge to its practical application. Here, a simple method is developed for improving the electrochemical performance of Na_xCl by controlling the upper limit of cut-off voltage. It is demonstrated that additional Na-vacancy defects can be introduced in the NaCl structure during the high-voltage activation process at 4.5 V. The structure then accommodates more sodium ions during the next discharge, resulting in increased capacity. At the same time, Cl-ions released by NaCl decomposition are oxidized to form Cl-based organic species at the active material interfaces. This plays a crucial role in protecting the NaCl electrode from undesired side reactions at high voltage. In short, this control of the charging protocol helps to induce more vacancies in the NaCl structure, as well as form stable interphases on the electrode surface, contributing to the increased capacity and enhanced cycle stability. This study will help in exploring a new approach for developing low-cost and high-capacity electrode material, which can potentially be applied in future energy-storage systems.

1. Introduction

Owing to the fast-growing markets for large-scale energy storage devices such as electric vehicle (EV) batteries and energy storage systems (ESSs), next-generation batteries with increased energy densities are in great demand.[1–4] Sodium is a highly sustainable, abundant resource in the Earth's crust, with a significantly lower cost than that of lithium. Thus sodium-ion batteries (SIBs) have been actively researched as promising candidates for next-generation batteries.[5–7] Significant efforts have been made to develop appropriate Na-host materials possessing fast Na^+ insertion/extraction ability, high specific capacity, and long-term cyclability.[5,8–11] An electrode with high structural stability during the repeated intercalation and deintercalation processes is a prerequisite for enabling highly reversible cycling in the Na-host material. Although various storage materials incorporating Na^+ have been reported, most of them unfortunately require high-cost and high-temperature synthesis processes,[12] which remains a critical drawback for SIB commercialization.

In the search for a promising cathode material for achieving efficient and low-cost SIBs, NaCl with electrochemically induced defects has been recently highlighted as a promising electrode material.[13] The precursor NaCl is by far the least expensive candidate material due to its ubiquitous presence in seawater. Thus, NaCl is believed to be ideal for large-scale application in EVs and ESSs. It has been demonstrated that electrochemically inactive NaCl can be activated by introducing structural defects and Na-ion vacancies, which drive a phase transition from B1- to B2-type NaCl in sodium-rich metallic Na_xCl ($x > 1$).[14–18] Electrochemically induced metallic Na_xCl exhibits a high initial capacity of ≈260 mAh g^{-1}; however, poor cycle stability with unsatisfactory capacity retention has been a major weak point.[13] Hence, a creative solution for improving the electrochemical performance is required for wide practical application of metallic Na_xCl, the least-expensive candidate material.

Here, we developed a simple method for enhancing the cycle stability and capacity retention of sodium-rich metallic Na_xCl ($x > 1$). We intentionally induced extra vacancy defects in the structure by simply controlling the voltage protocol; the

I. Moeez, D. Susanto, J.-H. Park, H.-D. Lim, K. Y. Chung
Energy Storage Research Center
Korea Institute of Science and Technology
Hwarang-ro 14-gil 5, Seongbuk-gu, Seoul 02792, Republic of Korea
E-mail: hdlim@kist.re.kr; kychung@kist.re.kr

J.-H. Park
Department of Materials Science and Engineering
Korea University
Seoul 02841, Republic of Korea

J.-Y. Kim
Advanced Analysis and Data Center
Korea Institute of Science and Technology
Hwarang-ro 14-gil 5, Seongbuk-gu, Seoul 02792, Republic of Korea

H.-D. Lim, K. Y. Chung
Division of Energy and Environment Technology
KIST School
Korea University of Science and Technology
Seoul 02792, Republic of Korea

The ORCID identification number(s) for the author(s) of this article can be found under https://doi.org/10.1002/adfm.202210370.

DOI: 10.1002/adfm.202210370

electrochemical activation step was carried out at the slightly increased voltage of 4.5 V, especially at the 2nd cycle. We confirmed that the excess deintercalation of Na ions caused additional Na−Cl bonds to break, where the extra Na vacancies in the metallic Na_xCl structure occurred. A relationship between the degree of electrochemical activation and structural stability of metallic Na_xCl was discovered, as well as the effect of generated Cl-based organic species on the electrode surface during the activation step. Various ex situ and in situ analyses were applied to investigate the influences of the additional Na vacancies and Cl-based organic species on the structural and compositional changes in the metallic Na_xCl.

2. Results and Discussion

Considering that the electrochemical introduction of vacancy defects in the inactive NaCl structure enables the intercalation of additional Na ions to form a sodium-rich metallic Na_xCl ($x > 1$) structure,[13] it was supposed that the use of the upper cut-off limit might induce more vacancy defects, thereby helping to improve the stability of the Na_xCl ($x > 1$) structure. Thus we carefully investigated the formation of vacancy defects in NaCl by changing the electrochemical testing protocol. To systematically demonstrate the effect of protocol controls, half-cells with NaCl (NC) electrodes were prepared and operated under different working voltages from 0.1 to 4.23 V (NC-4.23 V) and 0.1 to 4.5 V (NC-4.5 V), as shown in **Figure 1**. At the 1st cycle (activation cycle) (red lines in Figure 1a,c), each NC electrode was electrochemically charged up to 4.2 V at a 0.03 C to induce a partial B1- to B2-type NaCl phase transition, in a manner that was previously reported.[13] Then sodium ions were intercalated in the induced B2 phase during the subsequent discharge process, resulting in the formation of sodium-rich metallic Na_xCl ($x > 1$). At the 2nd cycle, different upper cut-off voltages were applied for NC-4.23 V (Figure 1a) and NC-4.5 V (Figure 1b): 4.23 V (dark yellow line) and 4.5 V (cyan line), respectively. When the high cut-off voltage was applied at the 1st charge step, the NaCl was prone to continued decomposition, quickly reaching cell failure (Figure S1, Supporting Information). Therefore, the high cut-off voltage was applied after the 1st activation cycle.

It should be noted that the overcharging activation at the 2nd cycle is a key strategy for improving the electrochemical performance of the NC electrode. The voltage profiles in Figure 1a show that the NC electrode (NC-4.23 V) delivered a high discharge capacity of 243 mAh g^{-1} at 0.03 C in the 1st discharge, which decreased to 175 mAh g^{-1} at the 2nd discharge. The discharge capacity gradually decreased as the cycle number increased, and the capacity retention of NC-4.23 V was only ≈7% after 50 cycles (inset of Figure 1a), demonstrating the poor cyclic stability of the NC electrode. In contrast, in the case of NC-4.5 V (Figure 1b) with the overcharging activation step, the initial discharge capacity was well maintained during cycling, showing a much-improved capacity retention of ≈57% (135 mAh g^{-1}) after 50 cycles at 0.03 C. Moreover, the NC-4.5 V electrode cycled at the increased current rate of 0.05 C (Figure 1c) exhibited capacity retentions of 70% and 45% (120 and 74 mAh g^{-1}) after 50 and 100 cycles, respectively, which significantly exceeded those of previously reported NaCl electrodes.[13] Furthermore, the effects of different upper cut-off

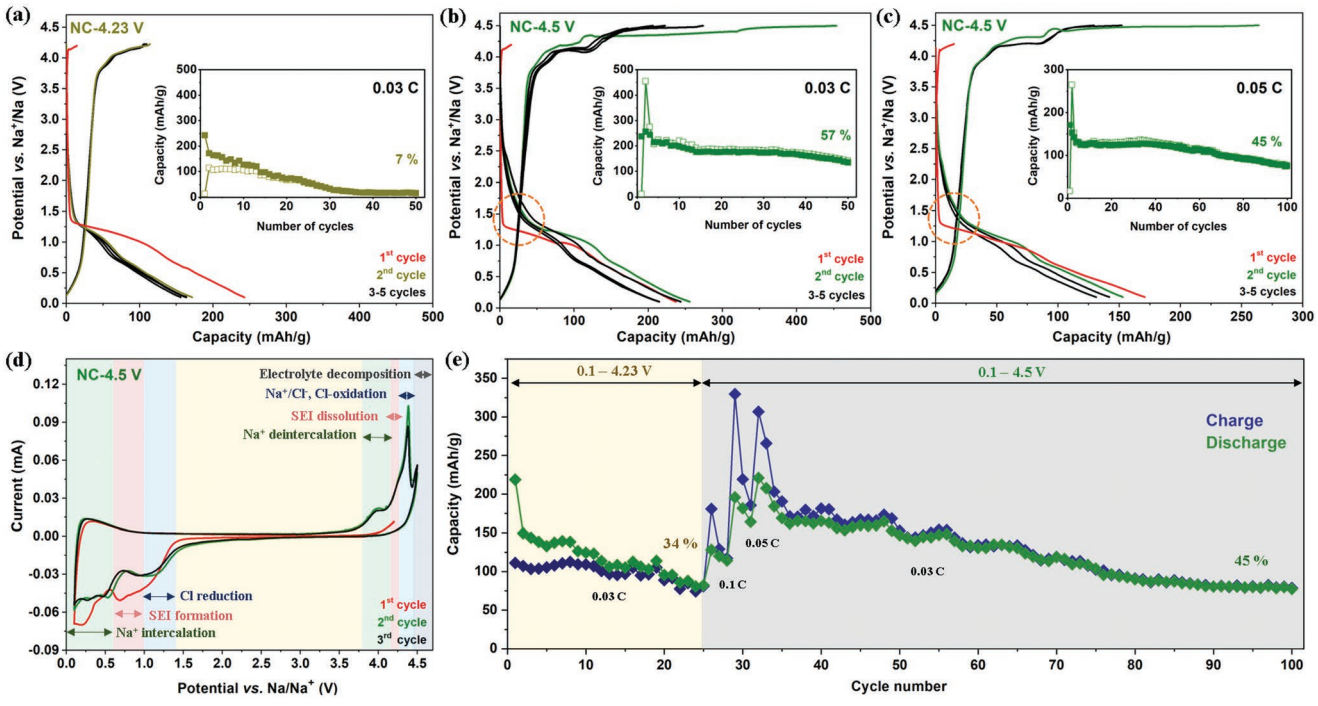

Figure 1. Comparison of voltage profiles of NaCl (NC) electrodes with working voltages in the range a) 0.1–4.23 V (NC4.23 V) and b) 0.1–4.5 V (NC-4.5 V) at 0.03 C; and c) NC-4.5 V cell at 0.05 C. The open and solid boxes represent charge and discharge capacities, respectively. d) Cyclic voltammetry measurement of NC electrode at 0.1 mV s^{-1}. e) Capacity retention test for NC half-cell cycled with two upper cut-off voltages: 0.1–4.23 V (light yellow region) for 25 cycles, and 0.1–4.5 V (light gray region) up to 100 cycles.

voltages such as 4.3 and 4.4 V are shown in Figure S2 (Supporting Information).

In order to closely investigate the effect of extra Na vacancies, cyclic voltammetry (CV) was performed for NC-4.5 V (Figure 1d). The CV profile for the 1st oxidation cycle exhibited an anodic peak at ≈4.2 V (red line in Figure 1d) corresponding to the partial B1- to B2-type NaCl phase transition after the introduction of vacancy defects in the structure.[13,19–22] In the next reduction process, two cathodic peaks were observed, for solid electrolyte interphase (SEI) formation (≈1.0 V) [10] and sodium intercalation into the NaCl structure (≈0.2 V) to form sodium-rich metallic Na_xCl.[13] During the 2nd oxidation step to 4.5 V (green line), two anodic peaks at 4.0 and 4.38 V were dominant, attributed to the deintercalation of sodium ions,[13,22] and further decomposition of NaCl, respectively. Moreover, a shoulder peak at 4.25 V reflected the dissolution of the interphase species [23,24] from the surface of the NC electrode, and the oxidation peak at 4.5 V was due to the oxidative decomposition of the electrolyte,[25] which is inconsistent with linear sweep voltammetry (LSV) curve in Figure S3 (Supporting Information). The CV curves indicate that there are additional sodium-ion extractions near 4.38 V, which could trigger the breaking of Na^+—Cl^- bonds, as well as induce additional vacancy defects. Then these vacancies helped accommodate excess sodium ions and form the sodium-rich compound (Na_xCl, x > 1) in the 2nd discharge. After the formation of extra vacancy defects during the overcharging activation, the CV profiles for the metallic Na_xCl became identically reversible, demonstrating that Na ions can be reversibly intercalated and deintercalated in the metallic-Na_xCl structure. To investigate the reaction kinetics, diffusion coefficients of NaCl electrodes and electrochemical impedance spectra (EIS) and during the cycling were analyzed and explained in Note S1 and Figure S4 (Supporting Information). The effect of induced extra vacancy defects was further investigated with a capacity retention test, as shown in Figure 1e. A half-cell with the NC electrode was operated in a voltage window between 0.1 and 4.23 V for 25 cycles, then the upper cut-off voltage was suddenly increased to 4.5 V (0.1–4.5 V) in order to induce the overcharging activation. As we expected, the initial 25 cycles resulted in a poor capacity retention of ≈34%. Notably, after the cut-off voltage was increased to 4.5 V at the 26th cycle, the capacity retention improved to 45% after 100 cycles. This demonstrates again that overcharging activation by controlling the cut-off voltage limit is an effective method for improving the retention capacity of the NC electrode.

To trace the extra vacancies induced during the overcharging activation, in situ XRD analysis was performed (**Figure 2**). In the XRD patterns, the dominant peaks (200) at 31.5° and (220) at 45.4° correspond to the B1(Fm-3m) phase of pristine NaCl, while the shoulder peak (110) at 45.1° (right panel of Figure 2a) indicates the phase transition from B1- to B2 (Im-3m)-type NaCl. In Figure 2a, the XRD patterns for the pristine NaCl, after the 1st charge to 4.2 V (State 1: 1C-4.2 V), and after the 1st discharge to 0.1 V (State 2: 1D-0.1 V) are displayed in black, orange, and green lines, respectively. Detailed in situ XRD patterns during State 1 and State 2 are provided in Figure S5 (Supporting Information), which demonstrate that the 1st charge to 4.2 V (the initial activation process) causes the partial phase transition from B1- to B2-NaCl, while the subsequent discharge to 0.1 V forms the sodium-rich metallic Na_xCl compound, as previously reported.[13] More importantly, while the in situ XRD patterns remain unchanged during the 2nd charge to 4.23 V

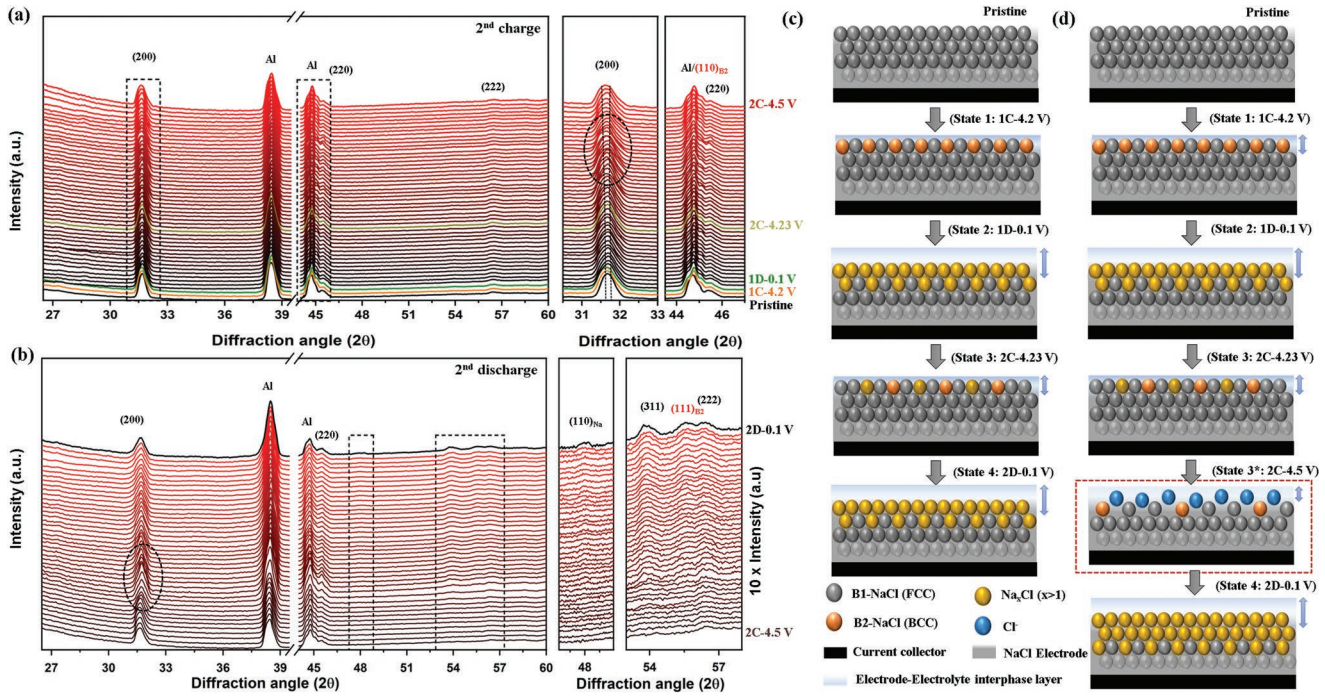

Figure 2. In situ XRD patterns of NC electrode during the initial two cycles: a) from pristine to State 3* (2C-4.5 V), and b) from State 3* (2C-4.5 V) to State 4 (2D-0.1 V). Schematic diagrams showing NC phase transitions and the formation of metallic sodium-rich Na_xCl (x>1) structure during electrochemical cycling for c) NC-4.23 V and d) NC-4.5 V.

(State 3: 2C-4.23 V, dark yellow line), a further increase to 4.5 V (State 3*: 2C-4.5 V) causes the $(200)_{B1}$ peak to broaden (marked in the black-dotted box at 31.7° and the right panel of Figure 2a). This is attributed to the additional vacancies generated during the overcharging activation. Furthermore, a decrease in the intensity of the $(200)_{B1}$ peak due to the partial decomposition of NaCl was observed. Ex situ XRD pattern observed at 4.23, 4.3, 4.4, and 4.5 V also confirmed that the intensities of the diffraction peaks decrease with increasing Na vacancy concentration in the structure (Figure S6, Supporting Information).[26,27] For the 2nd discharge (black line in Figure 2b, State 4: 2D-0.1 V), the dominant peaks at 48, 53.7, and 55.4° (marked in the black-dotted boxes and the right panel of Figure 2b) are matched to the sodium-rich metallic Na_xCl structure.[13] Also, the increase in the intensity of the $(200)_{B1}$ peak at 31.7° (black-dotted circle) indicates the recovery to the original NaCl state, confirming the high reversibility.[22,26] These results imply that the overcharging activation to 4.5 V at State 3*: 2C-4.5 V produced additional Na vacancies, which contributed to the increased discharge capacity. The results also confirmed the off-stoichiometric Na_xCl ($x > 1$) formation process was reversible.

We show the effects of cut-off control and the induced extra vacancy defects in the schematic diagrams of Figure 2c,d, and the voltage profiles at each step are provided in Figure S7 (Supporting Information). The conventional method, without overcharging activation is shown in Figure 2c and Figure S7a (Supporting Information). The activation process at the 1st charge (State 1: 1C-4.2 V) produced partial vacancy defects in the B1-NaCl structure and drove the phase transition from a B1- to B2-type NaCl structure. Then, during the discharge process (State 2: 1D-0.1 V), the electrochemically activated B2-NaCl phase accommodated sodium ions to form the sodium-rich phase (Na_xCl, $x > 1$). In the 2nd charge process to 4.23 V (State 3: 2C-4.23 V), Na ions were deintercalated from the structure, while the discharge to 0.1 V (State 4: 2D-0.1 V) enabled Na-ion intercalation. However, due to the limited extent of the phase transitions, it was difficult to fully form the sodium-rich phase inside the bulk particles. This confirmed the relatively low reversible capacity with poor cyclability shown in Figure 1a. In contrast, as shown in Figure 2d and Figure S7b (Supporting Information), when the overcharging activation to 4.5 V was applied at the 2nd cycle (marked by red-dotted box, State 3*: 2C-4.5 V), the additional breaking of Na—Cl bonds was also triggered, resulting in even more Na vacancies, and the formation of a second stage of sodium-rich metallic Na_xCl. This is why more Na ions were intercalated at the 2nd discharge (State 4: 2D-0.1 V in Figure 2d) than at the same state without the overcharging activation (State 4: 2D-0.1 V in Figure 2c).

To closely investigate the compositional and structural changes for the NC electrode caused by the overcharging activation process, soft X-ray absorption spectroscopy (XAS) was performed (**Figure 3**). Two typical detection modes (total fluorescence electron yield (TFY) and total electron yield (TEY), depending on the photon energies) were used to obtain detailed information about the bulk and surface of the NC electrode, respectively.[27] First, we focused on the structural changes in the bulk by using the TFY spectra (Figure 3a). The pristine NaCl (maroon-colored line) shows three distinct peaks at 1078.1, 1081.0, and 1088.7 eV corresponding to the NaCl structure.[28,29] While the overall intensities and shapes of the peaks remained unchanged after the 1st charge (State 1: 1C-4.2 V), the intercalation of sodium ions (Na—Na bonds at 1079.1, 1082.7, and 1087.6 eV) in the metallic Na_xCl structure[29] was observed after the 1st discharge at State 2: 1D-0.1 V. Then the 2nd charge process (State 3*: 2C-4.5 V) resulted in recovery to the original NaCl structure as indicated by the dark cyan line in Figure 3a. Moreover, the reappearance of Na—Na bonds after the 2nd discharge (State 4: 2D-0.1 V, orange line) was demonstrated, confirming the reversible reaction. Hence, the changes in the TFY-XAS intensities and line shapes clearly demonstrate that the overcharging activation step at the 2nd cycle formed metallic Na_xCl, and the intercalation and deintercalation of Na ions occurred reversibly in the structure.

The surface characteristics of the NC electrode with the overcharging activation was also investigated by analyzing the XAS spectrum for the Na K-edge in TEY mode, as shown in Figure 3b. For the pristine electrode (the maroon-colored line), the three major absorption peaks at 1078.1, 1081.0, and 1088.7 eV correspond to NaCl.[28,29] For the 1st charge (State 1: 1C-4.2 V), the intensities of the NaCl peaks slightly decrease owing to the partial decomposition of NaCl. Moreover, for the discharged electrodes (State 2: 1D-0.1 V and State 4: 2D-0.1 V), the peak heights near 1078.7 and 1086 eV increased due to the formation of interphase NaF and Na_2CO_3 species at the surface, respectively. It should be noted that the newly generated interphase acted as a cation transmitter, as well as electronic insulator.[25] For NC-4.5 V (State 3*: 2C-4.5 V in Figure 3a), the overall shapes of the Na K-edge TEY spectrum correspond to pristine NaCl; however, there was peak noise due to the partial decomposition and relatively low concentration of NaCl at the surface[30,31] compared to that of the bulk. Furthermore, the Na K-edge TEY-XAS spectrum for State 4: 2D-0.1 V is well matched with that of State 2: 1D-0.1 V. This again confirmed the recovery to the original NaCl structure along with the formation of the metallic Na_xCl structure (Figure 3a), as we described for Figure 2d.

To focus on the newly generated interphase layer at the discharge states (State 2: 1D-0.1 V and State 4: 2D-0.1 V), C and O K-edge XAS spectra in TEY mode were obtained (Figure 3c,d, respectively). It should be noted that, for the discharged electrodes (State 2: 1D-0.1 V and State 4: 2D-0.1 V), the appearance of a new peak related to Na_2CO_3 at 290.8 eV in the C K-edge spectrum in Figure 3c provides information about the formation of the surface interphase species. Importantly, the amount of the interphase species decreases at the charged states. This means that the interphase species were reversibly formed and dissolved according to the discharged and charged states, respectively. Furthermore, the dominant C—C bond (at 285.7 eV) and $-CH_2$ (at 288.9 eV) observed in the XAS spectra for the pristine NaCl and State 1: 1C-4.2 V electrodes correspond to electrode components (carbon black and binder).[32] Interestingly, the peaks related to the electrode components exhibited reverse trends compared to those of the interphase Na_2CO_3 materials. The intensities of the peaks decreased at discharged States 2 and 4, indicating the coverage of the bare surface of the NC electrode by the formed interphase layer.[10,25,33,34] The reappearance of these peaks for State 3*: 2C-4.5 V confirms again that the interphase layer dissolves at high voltage during charge, and reversibly reforms during the subsequent discharge.

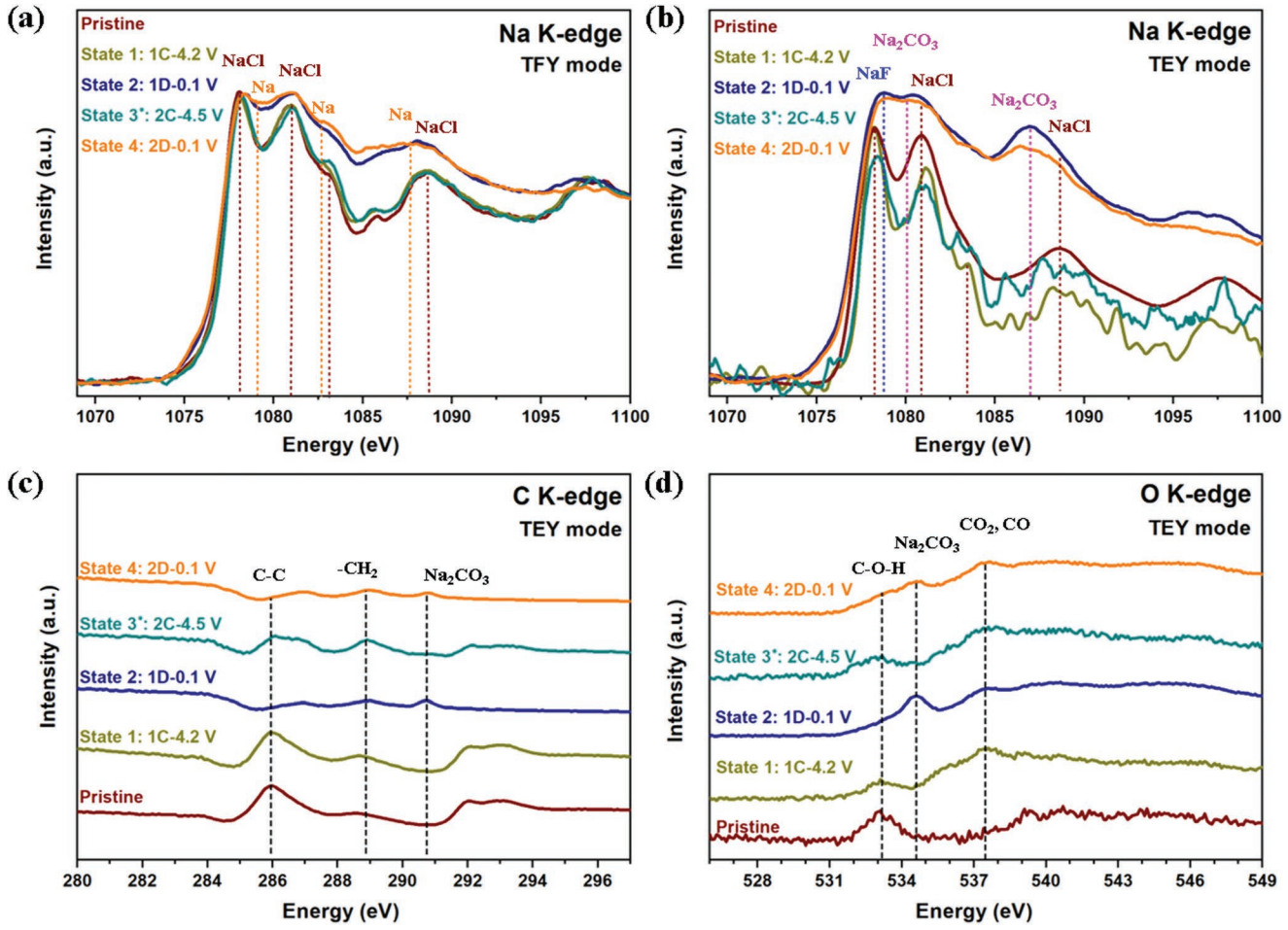

Figure 3. XAS absorption spectra obtained at Na K-edge for the NC pristine and various states from 1 to 4: a) total fluorescence yield (TFY) and b) total electron yield (TEY) modes. XAS spectra of c) carbon K-edge and d) oxygen K-edge in TEY mode for NC electrode.

Similar trends for the peak changes were identified in the O K-edge XAS spectrum (Figure 3d). The amount of Na_2CO_3 interphase material (534.5 eV) increased at each discharged state, and decreased at each charge state. Also, the cell components (C—O—H from the polyvinylidene fluoride (PVDF) binder) (at 533.1 eV) and oxygenated species (—CO, —CO_2) at 537.5 eV in Figure 3d[29,34,37,38] exhibited the opposite trend to that of the interphase material, revealing that the interphase species were formed and dissolved according to the discharged and charged states, respectively. Additional discussion is provided with the scanning electron microscope (SEM) and energy dispersive X-ray spectroscopy (EDS) element mapping results (Figure S8, Supporting Information). In short, two conclusions were made from the XAS analyses of the overcharging activation: first, additional NaCl bond-breaking was induced at 4.5 V, which enabled the formation of metallic Na_xCl in the subsequent discharge; and second, the formation of the interphase layer (SEI) was demonstrated, along with its reversible generation and dissolution during cycling.

To closely analyze the effects of NaCl decomposition and SEI dissolution at 4.5 V on the surface of the NC electrode, we performed X-ray photoelectron spectroscopy (XPS) and time-of-flight-secondary ion mass spectrometry (TOF-SIMS) analyses for the pristine and cycled NC electrodes, as shown in **Figure 4**. In the Cl 2p core-level spectra (Figure 4a) for the pristine electrode, two main peaks were detected at 198.7 and 200.3 eV ($\Delta E = 1.6$ eV) corresponding to the NaCl active material with Cl $2p_{3/2}$ and Cl $2p_{1/2}$ orbitals. For the 1st activation charge process (State 1:1C-4.2 V), there are shifts in the Cl peaks toward a lower energy level, implying the weakening of the Na—Cl bond. Also, at the discharged states (State 2: 1D-0.1 V and State 4: 2D-0.1 V), further peak shifts toward lower energy were observed, which confirms the presence of excess sodium atoms in the coordination sphere of chlorine in the sodium-rich metallic Na_xCl ($x > 1$).[13,35] It is worth noting that two additional peaks (200.4 and 202.0 eV) corresponding to the Cl $2p_{3/2}$ and Cl $2p_{1/2}$ orbitals of organic chlorine[36] were observed at State 3*: 2C-4.5 V. This might be due to the reaction between Cl ions released by NaCl bond breaking at 4.5 V and the electrolyte, resulting in the formation of a Cl-based interphase layer on the electrode surface. Notably, the Cl-based interphases were only detected after the overcharging activation process at the 2nd cycle, and they similarly disappeared at the discharge states (Figure 4a) as we observed in the XPS spectra at State 4: 2D-0.1 V. Additionally, the XPS spectra of O 1s, F 1s, and Cl 2p (Figure S9a,c, Supporting Information), again confirmed that the formation and

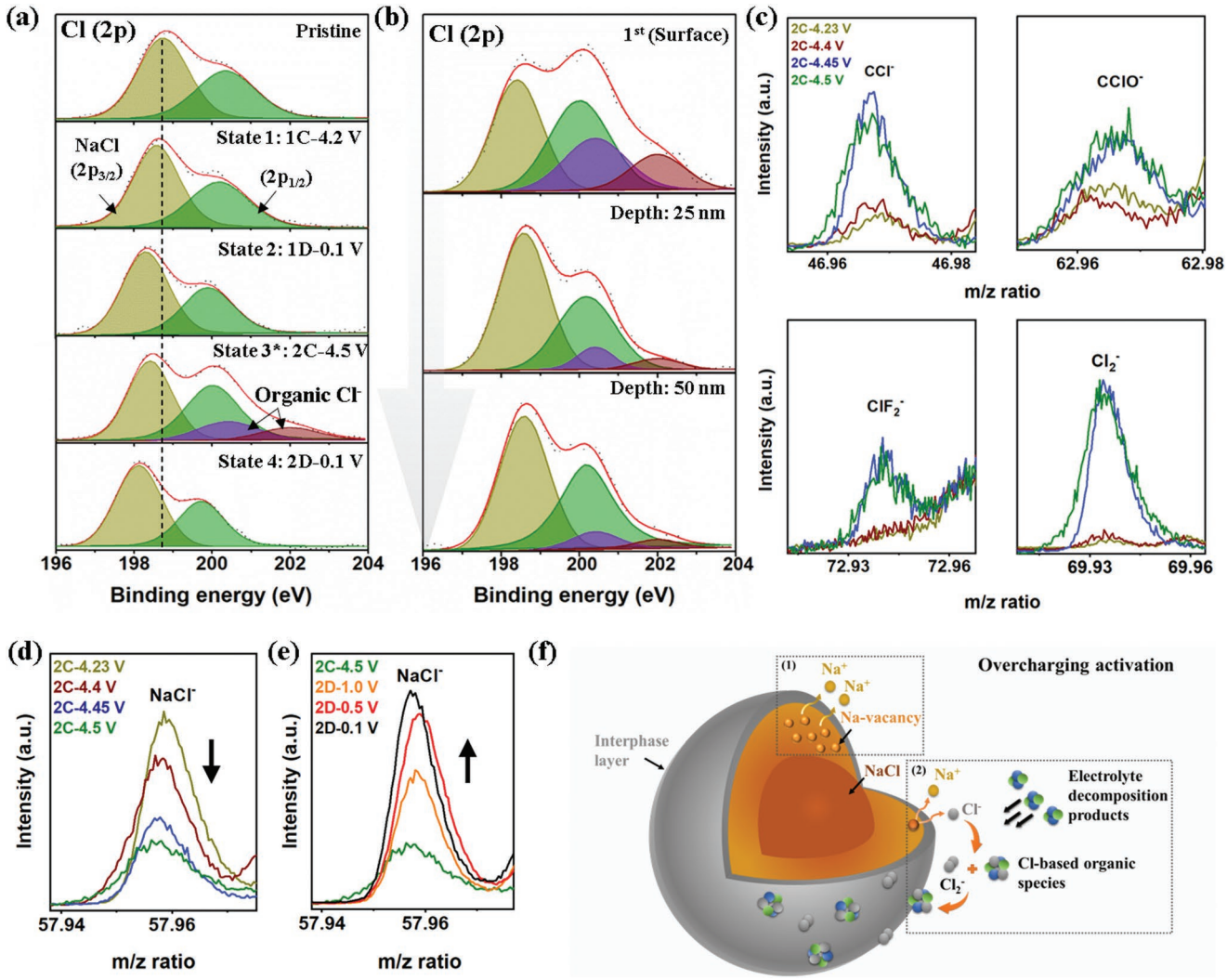

Figure 4. a) Comparison of Cl 2p XPS spectra for NC electrodes with various states from 1 to 4. b) XPS depth profile of Cl 2p for the State 3*: 2C-4.5 V. c) TOF-SIMS spectra for Cl- based organic species formed during 2nd charge process from State 3: 2C-4.23 V to State 3*: 2C-4.5 V. TOF-SIMS spectra of NaCl d) from State 3 (2C-4.23 V) to State 3*: 2C-4.5 V, and e) from State 3*: 2C-4.5 V to State 4: 2D-0.1 V. f) Schematic illustration showing the effect of overcharging activation process applied for the NC electrodes.

dissolution of the interphase layer occurred during the discharge and charge process, respectively. In order to determine whether these Cl-based species were mainly distributed on the surface, XPS depth profiling for the NC electrode at State 3*: 2C-4.5 V (Figure 4b) was performed. As the probe depth increased, the peak intensities related to the organic species at 200.4 and 202.0 eV decreased, which confirms that the Cl-based organic species existed primarily at the outer surface of the NC electrode. We believe that a key role of the Cl-containing passivating layer is protecting the NC electrode from undesirable side reactions, as well as the prevention of continuous electrolyte decomposition, especially at high voltages. Thus protection of the active material surface improved the structural stability at high voltage.

The Cl-based species compositions at the interphase layer were further studied with TOF-SIMS analyses for the pristine and cycled electrodes. As shown in Figure 4c, TOF-SIMS spectra were measured at various voltages (4.23, 4.4, 4.45, and 4.5 V), which were chosen between State 3: 2C-4.23 V and State 3*: 2C-4.5 V to investigate what occurs during the overcharging activation. It was observed that Cl-based organic species such as CCl^-, $CClO^-$, and ClF_2^-, together with the accumulation of Cl_2^- molecules, were especially dominant for 2C-4.45 V. The decomposition of NaCl and the formation of Cl_2^- fragments after the oxidation of Cl ions was similarly reported.[22] During the overcharging activation, Na^+ moved toward the negative electrode, while a spontaneous reaction simultaneously occurred between the Cl ions and electrolyte decomposition products, leading to the formation of CCl^-, $CClO^-$, and ClF_2^- at the interface. Thus the overcharging activation induced the breaking of Na—Cl bonds, and generated Cl ions ultimately contributed to the formation of the Cl-based organic interphase species. It is also worth noting that the overcharging activation process to 4.5 V initiated NaCl decomposition into Na^+ and Cl^-, as shown in the TOF-SIMS spectrum. Figure 4d shows the gradual decrease in NaCl as the charge increases from 4.23 to

4.5 V. These findings strongly support the fact that the formation of these Cl-based organic interphase species were triggered by NaCl decomposition. Also, NaCl was regenerated at the electrode interphase after the reduction of Cl-based organic interphase species during the subsequent discharge (Figure S10, Supporting Information), as shown by the TOF-SIMS spectra at various discharges (2D-1.0 V (orange line), 2D-0.5 V (red line), and 2D-0.1 V (black line)) (Figure 4e). This regeneration of NaCl explains the improved rechargeability of the NC electrode. On the other hand, TOF-SIMS spectra for SEI layer species (Figure S11, Supporting Information) confirm that the SEI layer dissolves at high voltage during charge, and reversibly reforms during the subsequent discharge.

In Figure 4f, we summarized the effects of the cut-off control process: 1) The overcharging activation initiated the breaking of Na—Cl bonds and additional Na vacancies were generated. The extra vacancies helped to form the sodium-rich metallic Na_xCl, resulting in the increased reversible capacities. 2) Chemical reactions between the released Cl ions and electrolyte were triggered, leading to the formation of a protective layer primarily consisting of Cl-based organic species. This layer suppressed undesirable reactions at the interfaces, thereby contributing to the improved cycle stability.

3. Conclusion

We developed a simple and effective method for introducing additional vacancy defects in the NaCl structure by applying a high-voltage charging step at the 2nd cycle. The overcharging activation process successfully incorporated extra Na-vacancy defects in the structure, while a novel sodium-rich metallic Na_xCl phase enabled the accommodation of more Na ions, resulting in improved reversible capacity. At the same time, implementing this overcharging strategy provides another advantage by forming a protecting layer enriched with Cl-based organic species on the NC electrode. This passivating layer effectively protected the active material from side reactions, leading to the enhanced cycling stability. By simply controlling the charge protocol, we enabled the NC electrode to exhibit significantly improved retention after 50 cycles (57%), in contrast, only 7% was obtained in the pristine NC electrode that was not activated by overcharging. We believe that this simple strategy will provide new insight into the extensive use of low-cost sea salt (NaCl) in future large-scale applications.

4. Experimental Section

Electrochemistry: NaCl electrodes were prepared by mixing NaCl (Sigma–Aldrich, ACS reagent, >99%, Germany), acetylene black, and polyvinylidene difluoride (PVDF, Solef 6020, Solvay) with a mass ratio of 7:2:1. The prepared electrodes were roll-pressed and dried overnight in a vacuum oven at 80 °C before cell assembly. Each coin cell was assembled in a glovebox (MBRAUN UNIlab, Germany) filled with argon, and H_2O and O_2 controlled below 0.1 ppm. The electrolyte used was 1 M $NaClO_4$ with PC: FEC (98:2, by volume). Electrochemical tests were conducted using a multichannel battery tester (MACCOR 4000, USA) with a coin cell (CR2025). Cyclic voltammetry (CV), linear sweep voltammetry (LSV), and electrochemical impedance spectroscopy (EIS) tests were conducted using a Bio-Logic VMP3, France potentiostat/galvanostat. The initial voltage for the measurement was set to the open-circuit potential of each cell. The voltage ranges for CV and LSV were 0.1–4.5 V and 0.1–5.0 V, respectively, at a scan rate of 0.1 mV s^{-1}. For EIS, the high frequency was 1 MHz and the low frequency was 0.1 Hz.

Material Characterization: A Rigaku R-AXIS IV^{++} instrument (Mo Kα radiation, wavelength of 0.7107 Å) was used for ex situ and in situ X-ray diffraction (XRD) measurements. For in situ experiments, time-resolved X-ray diffraction (TR-XRD) was used. Two different half-cells were used to measure the in situ XRD patterns for the 1st and 2nd cycles at scan rate of 0.03 C. The start and stop angles were set to be 10°–90°, and data were collected at180 s intervals for each scan during the in situ XRD measurements. For the ex situ analyses, NaCl half-cells were dissembled in the argon-filled glovebox, and the electrodes were washed and dried inside the glove box for 3 h to clearly remove the electrolyte. After the drying, the electrodes were transferred into a vacuum chamber for a characterization. For the cross-sectional SEM images, ion milling system (Arblade 5000, Japan) was used to section the surface by applying an argon plasma ion beam. Scanning electron microscopy (SEM) images energy-dispersive X-ray spectroscopy (EDS) were obtained by field emission (FE)-SEM instrument; S-4200, Hitachi, Japan. The sample was observed with 15 kV acceleration voltage of an electron beam at a pressure of 10^{-7} torr. X-ray absorption spectroscopy (XAS) was performed using a 10 D magnet beamline at the Pohang Accelerator Laboratory (PAL) and all of the spectra were obtained in both surface-sensitive total electron yield (TEY) and bulk-sensitive total fluorescence yield (TFY) mode. The probing depths for TEY and TFY were ≈10 and 100 nm, respectively. Due to the unavailability of the energy range for Cl K-edge spectroscopy at PAL, X-ray photoelectron spectroscopy (XPS) instrument of PHI 5000 VersaProbe spectrometer (ULVAC-PHI) equipped with an Al Kα (1486.6 eV) monochromator was used to determine the chlorine (Cl) chemical composition. To conduct XPS analysis, each electrode at different charge and discharge states was washed and dried. The prepared electrode was clamped onto the XPS stage and transferred into the main chamber of XPS instrument for a characterization. Depth profile studies were also conducted using an Ar^+ ion (2 KeV incident energy) etching system. The NaCl surface was sputtered in an Ar atmosphere (under an ultrahigh vacuum of 2×10^{-7} Pa) at an etching rate of 25 nm min^{-1} based on SiO_2. The energies of the core-level spectra presented in this study were calibrated from the C 1s core-level peak of PVDF at a binding energy of 284.6 eV. For time-of-flight secondary ion mass spectrometry (TOF-SIMS) studies, an IONTOF instrument (Münster) was used, and secondary ions of interest were detected in negative polarity. The analysis chamber was maintained under an ultrahigh vacuum with a pressure below 2×10^{-9} mbar. A pulsed 30 keV and 0.6 pA Bi_3^+ (9 ns)-ion beam set in spectrometry mode was applied to measure the spectrum for a raster size of 100 × 100 µm.

Supporting Information

Supporting Information is available from the Wiley Online Library or from the author.

Acknowledgements

This work was supported by the National Research Foundation of Korea (NRF-2022M3J1A1054151) funded by the Ministry of Science and ICT, and the KIST Institutional Program (2E31861 and 2V09335).

Conflict of Interest

The authors declare no conflict of interest.

Data Availability Statement

The data that support the findings of this study are available from the corresponding author upon reasonable request

Keywords

capacity retention, metallic NaCl, NaCl electrodes, Na-ion Batteries, sea salts

Received: September 6, 2022
Revised: October 30, 2022
Published online: November 27, 2022

[1] C. Zou, Q. Zhao, G. Zhang, B. Xiong, *Nat. Gas Ind.* **2016**,*3*, 1.
[2] D. P. Tabor, L. M. Roch, S. K. Saikin, C. Kreisbeck, D. Sheberla, J. H. Montoya, S. Dwaraknath, M. Aykol, C. Ortiz, H. Tribukait, C. Amador-Bedolla, C. J. Brabec, B. Maruyama, K. A. Persson, A. Aspuru-Guzik, *Nat. Rev. Mater.* **2018**, *3*, 5.
[3] D. Mignard, *Int J Environ Stud* **2014**, *71*, 796.
[4] F. Li, Z. Wei, A. Manthiram, Y. Feng, J. Ma, L. Mai, *J. Mater. Chem. A* **2019**, *7*, 9406.
[5] S. Paul, *J. Electrochem. Sci. Technol.* **2016**, *7*, 115.
[6] J. Y. Hwang, S. T. Myung, Y. K. Sun, *Chem. Soc. Rev.* **2017**, *46*, 3529.
[7] J. B. Goodenough, *J. Solid State Electrochem.* **2012**, *16*, 2019.
[8] Y. Li, Y. Lu, C. Zhao, Y. S. Hu, M. M. Titirici, H. Li, X. Huang, L. Chen, *Energy Storage Mater.* **2017**, *7*, 130.
[9] J. Li, S. L. Glazier, J. Paulsen, J. R. Dahn, X. Ma, J. Harlow, *J. Electrochem. Soc.* **2018**, *165*, A3195.
[10] Y. Huang, L. Zhao, L. Li, M. Xie, F. Wu, R. Chen, *Adv. Mater.* **2019**, *31*, 1808393.
[11] C. Fang, Y. Huang, W. Zhang, J. Han, Z. Deng, Y. Cao, H. Yang, *Adv. Energy Mater.* **2016**, *6*, 1501727.
[12] J. Deng, W. Bin Luo, S. L. Chou, H. K. Liu, S. X. Dou, *Adv. Energy Mater.* **2018**, *8*, 1701428.
[13] I. Moeez, H.-D. Lim, J.-H. Park, H.-G. Jung, K. Y. Chung, *ACS Energy Lett.* **2019**, *4*, 2060.
[14] G. Rajagopal, R. N. Barnett, U. Landman, *Phys. Rev. Lett.* **1991**, *67*, 727.
[15] J. L. Feldman, B. M. Klein, M. J. Mehl, H. Krakauer, *Phys. Rev. B* **1990**, *42*, 2752.
[16] R. N. Barnett, H. P. Cheng, H. Hakkinen, U. Landman, *J. Phys. Chem.* **1995**, *99*, 7731.
[17] G. Saleh, A. R. Oganov, *Phys. Chem. Chem. Phys.* **2016**, *18*, 2840.
[18] W. Zhang, A. R. Oganov, A. F. Goncharov, Q. Zhu, S. E. Boulfelfel, A. O. Lyakhov, E. Stavrou, M. Somayazulu, V. B. Prakapenka, Z. Konopkova, *Science* **2013**, *342*, 1502.
[19] G. Zhu, X. Tian, H. C. Tai, Y. Y. Li, J. Li, H. Sun, P. Liang, M. Angell, C. L. Huang, C. S. Ku, W. H. Hung, S. K. Jiang, Y. Meng, H. Chen, M. C. Lin, B. J. Hwang, H. Dai, *Nature* **2021**, *596*, 525.
[20] S. Devani, J. Anwar, *J. Chem. Phys.* **1996**, *105*, 3215.
[21] S. Guo, Q. Li, P. Liu, M. Chen, H. Zhou, *Nat. Commun.* **2017**, *8*, 845.
[22] T. Kinoshita, T. Mashimo, K. Kawamura, *J. Phys.: Condens. Matter* **2005**, *17*, 1027.
[23] S. Doubaji, B. Philippe, I. Saadoune, M. Gorgoi, T. Gustafsson, A. Solhy, M. Valvo, H. Rensmo, K. Edström, *ChemSusChem* **2016**, *9*, 97.
[24] W. Li, A. Dolocan, P. Oh, H. Celio, S. Park, J. Cho, A. Manthiram, *Nat. Commun.* **2017**, *8*, 14589.
[25] J. Song, B. Xiao, Y. Lin, K. Xu, X. Li, *Adv. Energy Mater.* **2018**, *8*, 1703082.
[26] Z. Qiao, L. Lin, X. Yan, W. Guo, Q. Chen, Q. Xie, X. Han, J. Lin, L. Wang, D. L. Peng, *Chem. - Asian J.* **2020**, *15*, 3620.
[27] J. D. Makinson, J. S. Lee, S. H. Magner, R. J. De Angelis, W. N. Weins, A. S. Hieronymus, *Adv. X-Ray Anal.* **2000**, *42*, 407.
[28] G. Shi, L. Chen, Y. Yang, D. Li, Z. Qian, S. Liang, L. Yan, L. H. Li, M. Wu, H. Fang, *Nat. Chem.* **2018**, *10*, 776.
[29] A. Di Cicco, A. Giglia, R. Gunnella, S. L. Koch, F. Mueller, F. Nobili, M. Pasqualini, S. Passerini, R. Tossici, A. Witkowska, *Adv. Energy Mater.* **2015**, *5*, 1500642.
[30] G. J. McIntosh, A. Chan, *Phys. Chem. Chem. Phys.* **2018**, *20*, 24033.
[31] C. Zheng, K. Mathew, C. Chen, Y. Chen, H. Tang, A. Dozier, J. J. Kas, F. D. Vila, J. J. Rehr, L. F. J. Piper, K. A. Persson, S. P. Ong, *NPJ Comput Mater* **2018**, *4*, 12.
[32] Y. Wen, Z. Wei, C. Ma, X. Xing, Z. Li, D. Luo, *Nanomaterials* **2019**, *9*, 775.
[33] A. Stamatelatos, P. Poulopoulos, A. Goschew, P. Fumagalli, E. Sarigiannidou, L. Rapenne, C. Opagiste, S. Grammatikopoulos, F. Wilhelm, A. Rogalev, *Sci. Rep.* **2019**, *9*, 13137.
[34] S. J. Rezvani, F. Nobili, R. Gunnella, M. Ali, R. Tossici, S. Passerini, A. Di Cicco, *J. Phys. Chem. C* **2017**, *121*, 26379.
[35] B. V. Ratnakumar, M. C. Smart, S. Surampudi, *J. Power Sources* **2001**, *97*, 137.
[36] A. Wang, S. Kadam, H. Li, S. Shi, Y. Qi, *NPJ Comput Mater* **2018**, *4*, 15.
[37] Y. Li, F. Wu, Y. Li, M. Liu, X. Feng, Y. Bai, C. Wu, *Chem. Soc. Rev.* **2022**, *51*, 4484.
[38] H. Ren, L. Zheng, Y. Li, Q. Ni, J. Qian, Y. Li, Q. Li, M. Liu, Y. Bai, S. Weng, X. Wang, F. Wu, C. Wu, *Nano Energy* **2022**, *103*, 107765.